ACS OMEGA

http://pubs.acs.org/journal/acsodf

Article

Dabrafenib–Panobinostat Salt: Improving the Dissolution Rate and Inhibition of BRAF Melanoma Cells

Sunil K. Rai,* Gaetano Marverti, Anilkumar Gunnam, Suryanarayana Allu, and Ashwini K. Nangia*

Cite This: *ACS Omega* 2023, 8, 18255–18265

Read Online

ACCESS | Metrics & More | Article Recommendations | Supporting Information

ABSTRACT: Cocrystallization of the drug–drug salt-cocrystal of the histone deacetylase inhibitor (HDACi) panobinostat (PAN) and b-rapidly accelerated fibrosarcoma (BRAF) inhibitor dabrafenib (DBF) afforded single crystals of a two-drug salt stabilized by N^+–H···O and N^+–H···N^- hydrogen bonds between the ionized panobinostat ammonium donor and dabrafenib sulfonamide anion acceptor in a 12-member ring motif. A faster dissolution rate for both drugs was achieved through the salt combination compared to the individual drugs in an aqueous acidic medium. The dissolution rate exhibited a peak concentration (C_{max}) of approximately 310 mg cm^{-2} min^{-1} for PAN and 240 mg cm^{-2} min^{-1} for DBF at a T_{max} of less than 20 min under gastric pH 1.2 (0.1 N HCl) compared to the pure drug dissolution values of 10 and 80 mg cm^{-2} min^{-1}, respectively. The novel and fast-dissolving salt DBF^-·PAN^+ was analyzed in $BRAF^{V600E}$ melanoma cells Sk-Mel28. DBF^-·PAN^+ reduced the dose–response from micromolar to nanomolar concentrations and lowered IC_{50} (21.9 ± 7.2 nM) by half compared to **PAN** alone (45.3 ± 12.0 nM). The enhanced dissolution and lower survival rate of melanoma cells show the potential of novel DBF^-·PAN^+ salt in clinical evaluation.

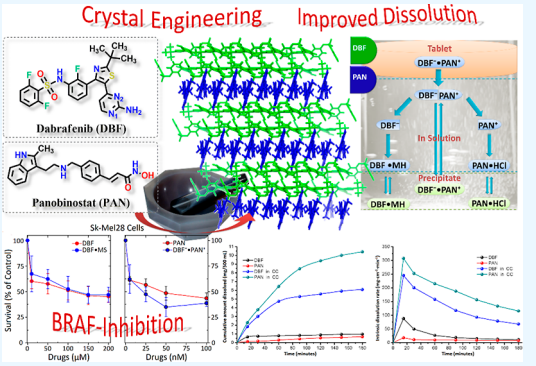

1. INTRODUCTION

Chronic diseases are not only the outcome of abnormalities in our genes but also a result of lifestyle and environmental factors.[1] Among the multifactorial diseases,[2−4] cancer is the second-most killer disease worldwide after cardiovascular ailments.[5,6] Skin cancer is one of the most common forms of human cancer, which is broadly classified as melanoma and nonmelanoma.[7,8] Specifically, metastatic melanoma is a lethal form and one of the fastest-growing incidences.[9] The emphasis on cancer diagnosis, prevention, and treatment (i.e., surgery, radiation, and chemotherapy) is specific to the type of cancer.[10,11] Among these, chemotherapy is the first-line treatment for most cancers even as more targeted therapies are moving forward in research and clinical application.[12−14] The most successful targeted therapies are chemical drugs which attack a specific protein or enzyme by carrying out a mutation or genetic alteration that is specific to the cancer cells but not to the normal host tissue.[15,16] More than 60% of all melanoma cases are due to activation of mutations in the b-rapidly accelerated fibrosarcoma (BRAF) protein which is responsible for directing cell growth.[17] The B-Raf mutant cancer, or $BRAF^{V600E}$ mutation, which renders the kinase constitutively active, is very common.[18] Clinical research suggests that small-molecule inhibitors offer a novel, targeted approach for the treatment of $BRAF^{V600E}$-pathway cancers.[19] The approval of selective BRAF inhibitors (BRAFis) vemurafenib and dabrafenib revolutionized advanced melanoma therapy with an improved response rate and overall survival compared to standard chemotherapy.[19−21] Although mutant BRAFis have achieved unprecedented clinical responses in the treatment of melanomas with activating mutations in $BRAF^{V600E}$, yet complete remission is rarely observed.[22] However, responses are commonly short-lived with most patients relapsing within 1 year which is indicative of acquired drug resistance in melanoma cells.[23]

The combination of anticancer drugs with other chemotherapeutic agents has shown an advantage over monotherapy for the treatment of cancers.[24,25] In a very recent example, a combination of dabrafenib and trametinib was approved in May 2018 by the U.S. Food and Drug Administration (US-FDA) for the treatment of metastatic anaplastic thyroid cancer with $BRAF^{V600E}$ or $BRAF^{V600K}$ mutations.[26,27] Ongoing clinical trials of the histone deacetylase inhibitor (HDACi) and mutant BRAF inhibitor have shown synergistically induced cell death in $BRAF^{V600E}$ melanoma cells.[28,29] These combinations can be administered either separately in multiple doses or in fixed-dose combination (FDC) formulations. Hitherto, none of the combinations has been tested in the form of FDCs to evaluate

Received: March 20, 2023
Accepted: April 25, 2023
Published: May 8, 2023

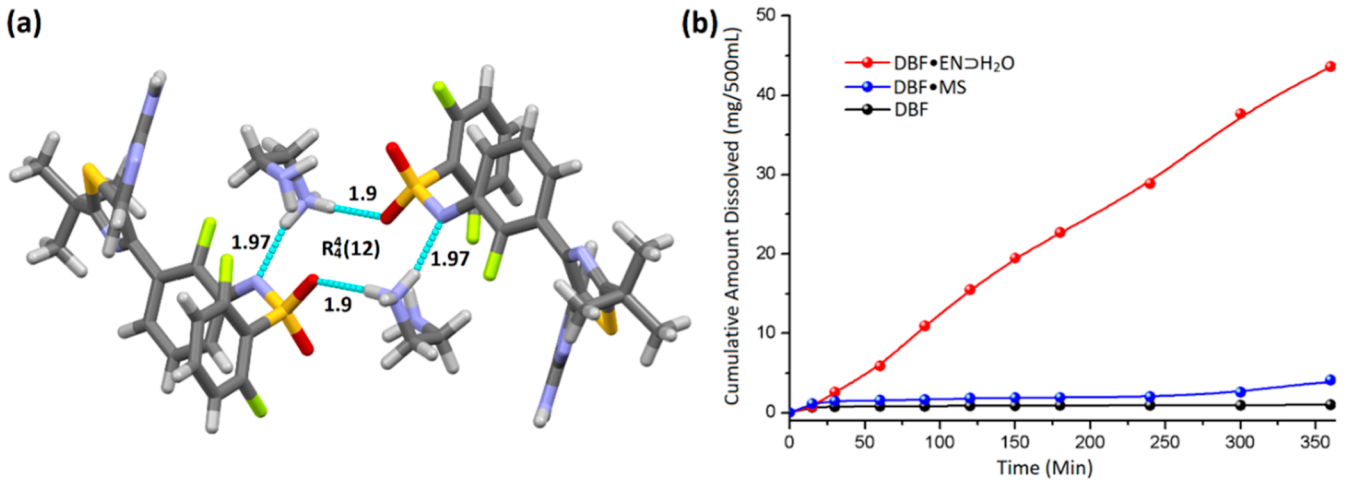

Figure 1. Representation of (a) 12-member ring motif $R_4^4(12)$ with $N^+-H\cdots O$ and $N^+-H\cdots N^-$ hydrogen bonds in DBF·EN⊃H_2O and (b) cumulative dissolution profile of DBF, DBF·EN⊃H_2O, and DBF·MS compared with other salts (for details, see ref 36). Copyright American Chemical Society, 2020.

the contribution to the combined effects. The search for new drug−drug combinations[30] of already approved or investigational drugs will save considerable cost and time because of their known performed pharmacokinetic and safety profiles,[31,32] thereby reducing the regulatory approval phase from ∼15 years to 5 years.[32] For example, the first salt-cocrystal category drug Entresto, valsartan−sacubitril trisodium hemi-pentahydrate, approved by the US-FDA in 2015,[33] shows superior drug response in chronic cardiac patients compared to valsartan alone.[34]

We report herein the crystalline salt of the BRAF inhibitor dabrafenib (DBF) and HDAC inhibitor panobinostat (PAN) and the role of the novel $DBF^-\cdot PAN^+$ salt to induce cell death in $BRAF^{V600E}$ melanoma as well as in other cancer cells. Another objective of the salt formulation is to improve the dissolution rate and solid form stability in a single tablet. The idea of dual improvement is inspired by the work of Lai et al.[35] and our recent work on high-solubility salts of dabrafenib salts with amines.[36] The combinations of HDACs and BRAFs inhibitors killed $BRAF^{V600E}$ melanoma cells by the induction of necrosis.[35] Rai et al.[36] recently reported X-ray crystal structures of dabrafenib with a variety of alkyl amines, all of which exhibited proton transfer from the acidic sulfonamide group to the amine conformer as $DBF^-\cdot NH^+$ salts. The salt structures are consistently sustained by a 12-member ring motif $R_4^4(12)$ with $N^+-H\cdots O$ and $N^+-H\cdots N^-$ hydrogen bonds (Figure 1a).[37] The dissolution rate of the DBF·EN⊃H_2O salt (DBF ethylene diamine hydrate) was observed to be much higher than that of DBF and the marketed mesylate salt (DBF·MS), and its cumulative dissolution profile is shown in Figure 1b.

2. RESULTS AND DISCUSSION

Based on the recurrence of $DBF^-\cdot NH^+$ salt structures,[36] we expected that the secondary amine group of PAN (Scheme 1) will form a salt with the sulfonamide group of DBF and the *N*-hydroxy amide group in PAN, and the amino-pyridine functional groups of DBF will form neutral hydrogen bonds, such as *N*-hydroxamic acid dimer and amino-pyridine dimer synthons.[38] The novel solid form of DBF and PAN was prepared in a 1:1 ratio by cogrinding in an agate mortar with a few drops of ethanol added for efficient mixing and homogenization (solvent drop grinding).[39] Formation of the

Scheme 1. Chemical Structure of DBF and PAN

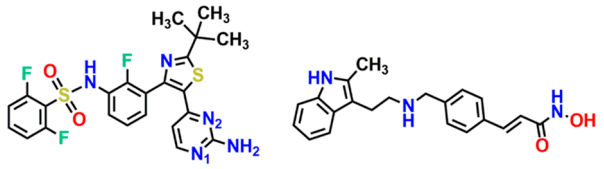

expected salt was checked by powder X-ray diffraction (PXRD) and differential scanning calorimetry (DSC). Furthermore, diffraction-quality single crystals of the salt were harvested from ethanol by slow evaporation of the solvent under ambient conditions.

2.1. Crystallographic Discussion. The X-ray crystal structure was solved in the triclinic crystal system of the $P\bar{1}$ space group with one molecule of each drug in the salt complex (Table S1 in the Supporting Information). The ORTEP diagram of $DBF^-\cdot PAN^+$ showed a clear proton transfer from the sulfonamide of DBF to the secondary aliphatic amine of PAN (Figure 2a). The molecular packing of DBF (green) and PAN (blue) is arranged in alternate layers in the crystal structure (Figure 2b). The acidic sulfonamide proton of DBF is transferred to the nitrogen atom of the secondary amine in PAN, and the sulfonamide anion in DBF^- and ammonium cation in PAN^+ construct the $R_4^4(12)$ ring motif (Figure 2c).[37] The positions of hydrogen atoms were confirmed from the difference in electron density Fourier maps (Figure S1 in the Supporting Information). The hydroxamic acid in PAN^+ forms a N−O−H···O homosynthon in the $R_2^2(10)$ ring motif which further extends through bifurcated hydrogen bonds on the oxygen atom with the N−H donor on the indole ring (Figure 2d). The N−H donor of hydroxamic acid bonds to the pyrimidine aromatic N acceptor of DBF, and the N−H donor of DBF interlinks DBF molecules through the sulfonamide O acceptor in the $R_3^3(12)$ ring motif. Apart from the hydrogen bonding and salt formation in $DBF^-\cdot PAN^+$, it is important to examine the intermolecular interactions in the 2-aminopyrimidine ring portion of DBF (Table S2 in the Supporting Information).[36] The supramolecular synthon formed between the 2-amonopyrimidine ring (i.e., $R_3^3(12)$ ring motif) where the ring nitrogen atom N1 appears to be free

https://doi.org/10.1021/acsomega.3c01881
ACS Omega 2023, 8, 18255−18265

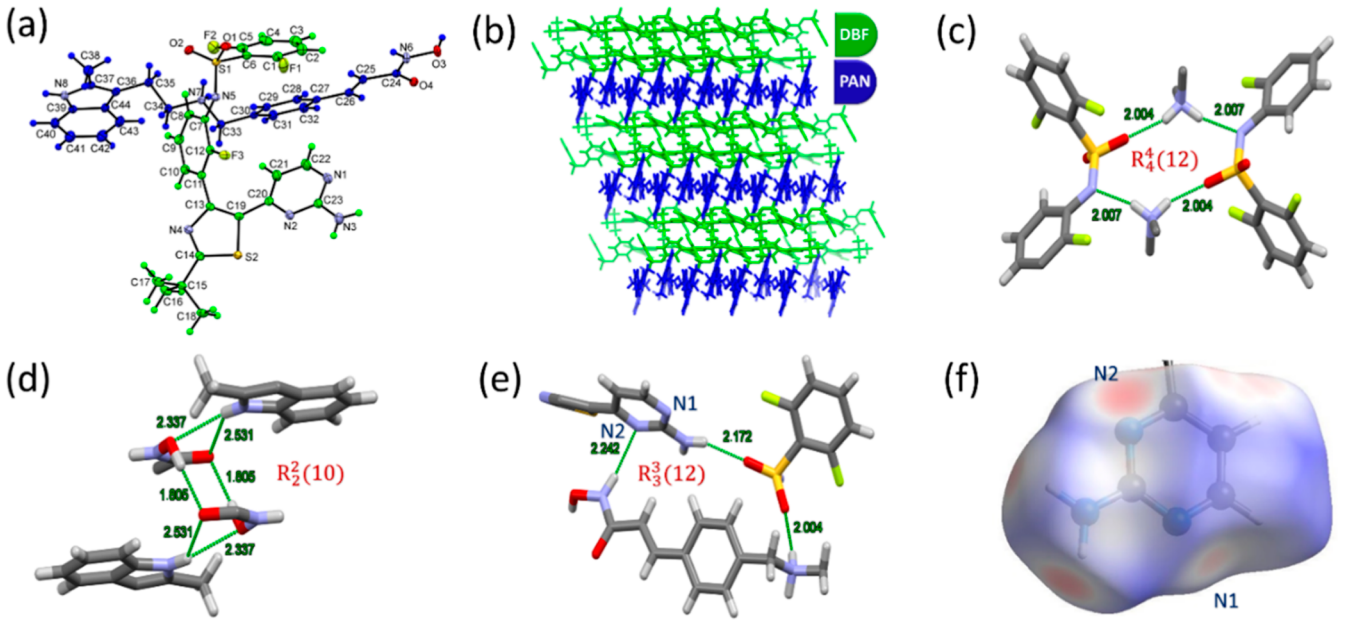

Figure 2. (a) ORTEP diagram of $DBF^-{\cdot}PAN^+$; thermal ellipsoids are drawn at the probability level of 50%, (b) molecular packing of the $DBF^-{\cdot}PAN^+$ salt in the crystal lattice, (c,–e) supramolecular synthons in the $DBF^-{\cdot}PAN^+$ salt, and (f) the Hirshfeld surface generated over d_{norm} around the 2-aminopyrimidine ring. For the sake of clarity, only selected fragments and atoms are shown.

from any strong interaction and N2 acting as a hydrogen bond acceptor is displayed in Figure 2e. Furthermore, the Hirshfeld surface analysis is performed around the 2-aminopyrimidine ring, and the surface is generated over d_{norm} to get quantitative information on hydrogen bond interactions (Figure 2f). It is clear from the intensity of red circular spots over d_{norm} that intermolecular interaction on the N1 atom is much weaker compared to the N2 atom. In fact, the N1 acceptor does not engage in any hydrogen bonding.

2.2. Thermal Analysis. The well-characterized novel salt $DBF^-{\cdot}PAN^+$ was prepared for cell-line experiments by mechanochemical grinding, and the bulk phase was matched with the crystal structure (Figure S2 in the Supporting Information). DSC analysis of the crystalline phase (from an X-ray quality crystal batch) showed a melting endotherm at 210 °C with an immediate decomposition thereafter. A solid–solid phase transition was observed before melting at 157 °C (Figure S3 in the Supporting Information). Before thermal analysis of a scale-up batch of $DBF^-{\cdot}PAN^+$, DSC-TGA of DBF and PAN-free bases were analyzed. It was found that the isolated DBF-free base (prepared from its mesylate salt) is an anhydrous form with the melting endotherm at 217 °C (Figure 3a). However, the commercial PAN-free base showed water content equivalent to a monohydrate with a weight loss of ∼4.8% (calculated = 4.9%), and a corresponding broad endotherm ranging ca. 65–105 °C was observed in DSC which melted at 156 °C, followed by immediate decomposition (Figure 3c). A small, broad endotherm was observed for the $DBF^-{\cdot}PAN^+$ salt between 50 and 100 °C and then melting at 204 °C followed by immediate decomposition of the salt starting at 207 °C (Figure 3e). Thermal analysis of the individual drugs and the salt residue after dissolution/solubility experiments in a slurry medium is analyzed in the next section.

2.3. Dissolution, Solubility, and Phase Changes. Dissolution is the first step for a solid dosage form for the release of the drug in solution and thus directly impacts bioavailability.[40] Analysis of the equilibrium solubility and phase stability of the solid form is also important to understand the release of the drug in the dissolution/solubility media. Therefore, prior to dissolution measurements, the preparation of the $DBF^-{\cdot}PAN^+$ salt was scaled up using the ethanol drop grinding method, and its phase purity was checked by PXRD profile fitting. Equilibrium solubility of the salt form and individual free bases was performed followed by characterization of the leftover solid forms at the end of the dissolution experiment. Here, all solubility and dissolution experiments were performed under a pH 1.2 aqueous medium (0.1 N HCl). The solid residue isolated after the dissolution experiment (3 h duration) matched with the starting crystal form, but the nature of the residue after equilibrium solubility time (24 h) in the slurry medium showed a different PXRD pattern for the individual drugs, namely, DBF and PAN (Figure 4a,b). In contrast, the PXRD profile fitting of the $DBF^-{\cdot}PAN^+$ salt showed an excellent match of the bulk as-prepared material and the crystalline solid after dissolution and equilibrium slurry experiment (Figure 4c,d and Figures S8–S11 in the Supporting Information). DSC of the solid residue after equilibrium solubility/slurry experiments showed minor variations compared to the as-prepared scaled-up form, wherein phase transition was observed in the range of ca. 100–120 °C (Figure 3f), which could be due to higher crystalline content after slurring (aggregation) compared to the product immediately after mechanochemical preparation (micronization) ca.65–105 °C (Figure 3e). There was no phase change observed in the PXRD pattern after the slurry experiment, which indicates that the crystalline $DBF^-{\cdot}PAN^+$ salt form is stable in aqueous ambient conditions (Figure 4c,d). A thorough characterization of drug phases was performed using thermal techniques and electron microscopy. TGA of the new solid phase of DBF showed a weight loss of ca. 3.5%, and corresponding to this temperature, a broad endotherm was observed between 110 and 150 °C in the DSC thermogram followed by a melting endotherm at 214 °C (Figure 3b). However, the melting endotherm peak for the DBF-free base

https://doi.org/10.1021/acsomega.3c01881
ACS Omega 2023, 8, 18255–18265

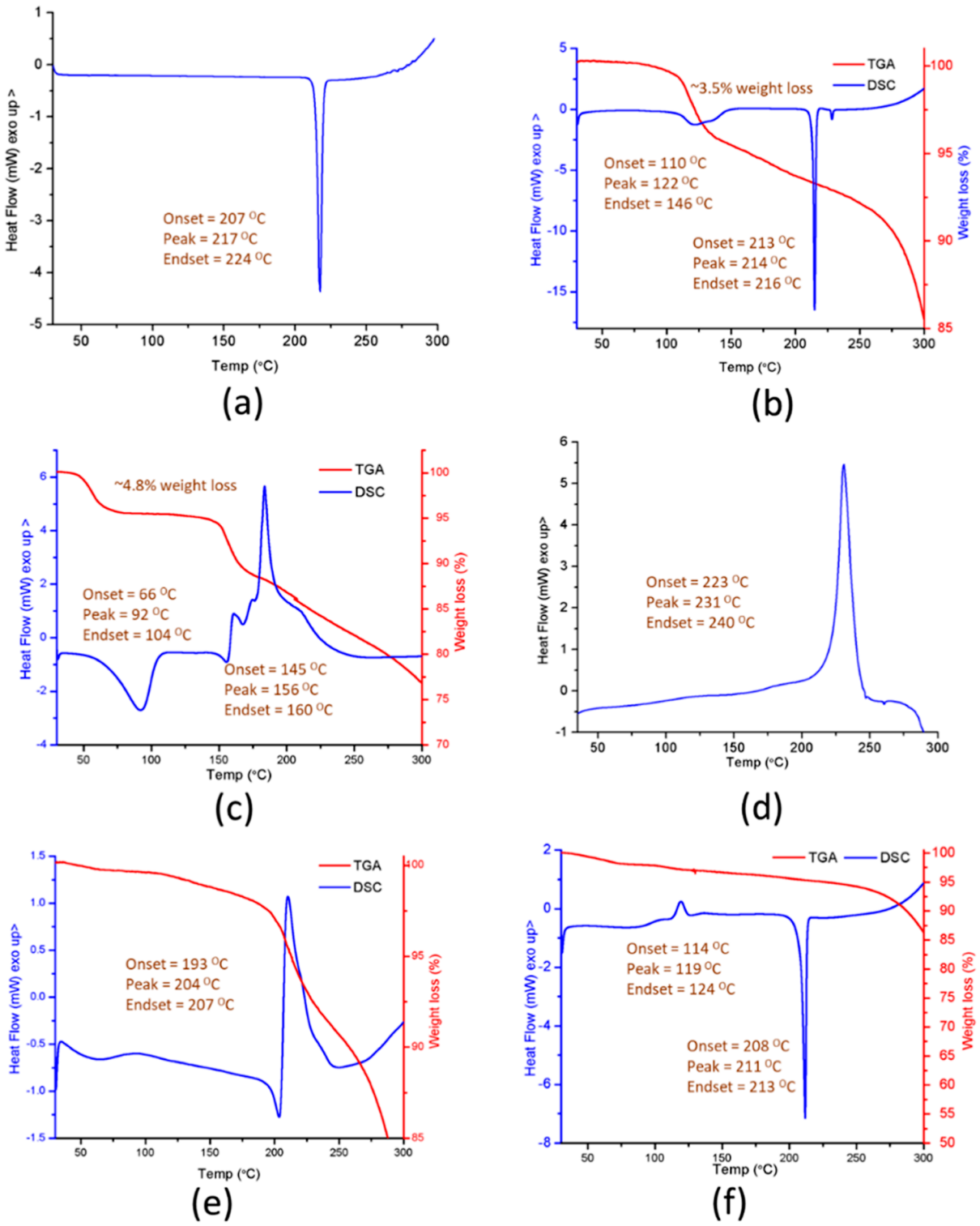

Figure 3. DSC and TGA thermograms. (a) DSC thermogram of the DBF-free base, (b) DSC and TGA overlay of the undissolved DBF residue from the equilibrium slurry medium at pH 1.2, (c) DSC and TGA thermogram overlay of the PAN-free base, (d) DSC thermogram of undissolved PAN from the equilibrium slurry medium at pH 1.2, (e) DSC and TGA thermogram overlay of the $DBF^{-}{\cdot}PAN^{+}$ scale-up batch, and (f) DSC and TGA thermogram overlay of undissolved $DBF^{-}{\cdot}PAN^{+}$ under the equilibrium slurry medium at pH 1.2.

showed only one endotherm at 217 °C (Figure 3a). Additional thermal DSC, TGA plots (Figures S4−S6), and PXRD overlay diffractograms (Figures S7−S11) for the three crystalline drugs are shown in the Supporting Information. FESEM showed visible differences in the crystal morphology of both DBF forms where the DBF-free base exists as submicron size agglomerates of fine crystallites and the product phase isolated from the slurry has submicron size rhombus crystals (Figure 5a,b). Since DBF solid was incubated in an aqueous HCl buffer, the possibility of hydrochloride salt formation was checked by analyzing the chlorine content using EDX which showed a trace amount of chlorine. There is a possibility of

https://doi.org/10.1021/acsomega.3c01881
ACS Omega 2023, 8, 18255−18265

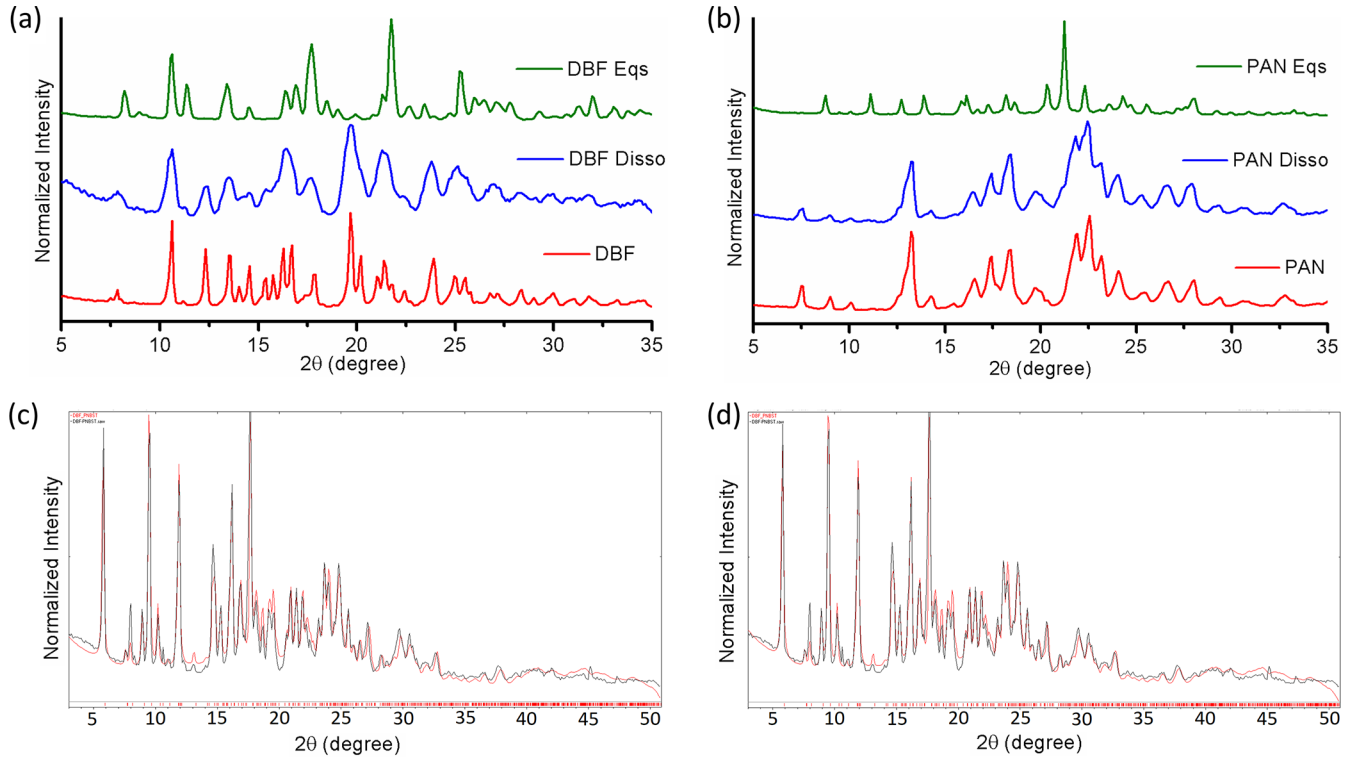

Figure 4. Overlay of PXRD patterns. (a) PXRD overlay of the DBF-free-base residue after dissolution and in the equilibrium slurry medium at pH 1.2, (b) PXRD overlay of the PAN-free base residue after dissolution and in the equilibrium slurry medium at pH 1.2, (c) PXRD profile fitting of $DBF^{-}{\cdot}PAN^{+}$ scale-up batch (black) matching with the single-crystal structure (red) (R_p = 13.68%, R_{wp} = 17.85%), and (d) PXRD profile fitting of the $DBF^{-}{\cdot}PAN^{+}$ residue after the dissolution experiment in an aqueous slurry medium at pH 1.2 (black) with the single-crystal structure (red) (R_p = 11.84%; R_{wp} = 16.31%).

HCl contamination, but there is no indication of any salt form (Figure 6a,b). TGA showed weight loss in the new solid phase of DBF corresponding to a monohydrate form (calculated water loss 3.35%, observed weight loss 3.5%, Figure 3b), named DBF·MH. A commercial PAN-free base is a monohydrate form (Figure 3c); however, the product solid isolated after the equilibrium solubility experiment showed a single exotherm in the DSC thermogram at ca. 230 °C (Figure 3d). The crystal morphology of the PAN monohydrate looked like sharp blades as observed by FESEM, while the new solid form showed an irregular morphology with coarse crystal surfaces (Figure 5c,d). The high melting point of the anhydrous new solid phase (231 °C) indicated the possibility of hydrochloride salt formation of PAN under an equilibrium solubility slurry medium. The EDX pattern of the product solid phase of PAN isolated from the equilibrium slurry flask showed a significant amount of chloride content (ca. 5.63% by weight and 2.2% by atomic; theoretical chloride in PAN·HCl ∼9.19% by weight and 1.96% by atomic) and indicated partial monohydrochloride salt formation (Figure 6c,d). The hydrochloride salt of PAN obtained from the equilibrium solubility medium was named PAN·HCl. These results suggest that in a strongly acidic medium, both DBF and PAN transform to a monohydrate and hydrochloride salt form, respectively, to some extent. Subsequently, equilibrium solubility measurements of the $DBF^{-}{\cdot}PAN^{+}$ salt were performed and the isolated solid residue showed an overlapping PXRD pattern by profile fitting with the X-ray crystal structure (Figure 4d), indicating phase stability of the multidrug salt. Although the scale-up batch and crystal form appeared to be the same crystalline phase by PXRD overlay, DSC showed a minor difference before the melting endotherm at 210 °C (Figure 3e,f). An endothermic phase transition at 157 °C was observed in the crystal form of the $DBF^{-}{\cdot}PAN^{+}$ salt (Figure S3 in the Supporting Information), whereas the salt obtained from the scale-up batch showed a small, broad endotherm between 50 and 100 °C (Figure 3e). These minor differences in the crystal form and mechanochemical preparation could be due to the inhomogeneous distribution of particle size and morphology during the scale-up batch.

The dissolution rate of $DBF^{-}{\cdot}PAN^{+}$ and individual drugs was measured under gastric pH 1.2 conditions (0.1 N HCl solution). The neat form of DBF and PAN (free base) show very poor dissolution, while gratifyingly, the $DBF^{-}{\cdot}PAN^{+}$ salt shows much faster drug dissolution (Figure 7a). The cumulative drug dissolved reaches a saturation value of 12.18 mg/L for DBF, while for PAN, there is a continuous increase of drug concentration (i.e., 4.60 mg/L at 15 min to 20.81 mg/L at 180 min) throughout the experimental time period of 3 h. Second, high C_{max} values were achieved within 20 min for $DBF^{-}{\cdot}PAN^{+}$ (310 mg cm^{-2} min^{-1} for PAN and 240 mg cm^{-2} min^{-1} for DBF). The intrinsic dissolution rate (IDR) of pure DBF is higher than that of pure PAN (Figure 7b). Equilibrium solubility experiments of DBF and PAN were carried out to know the possibility of phase conversion in a pH 1.2 medium. The PXRD analysis of residual precipitate shows that neat DBF converted to DBF·MH, which is comparatively less soluble (Figure S8 in the Supporting Information). It appears that the rate of dissolution of DBF from the salt pellet to the solution phase and rate of precipitation of DBF·MH reached a steady state immediately, and thus, the apparent dissolution rate showed a constant concentration throughout the experi-

https://doi.org/10.1021/acsomega.3c01881
ACS Omega 2023, 8, 18255−18265

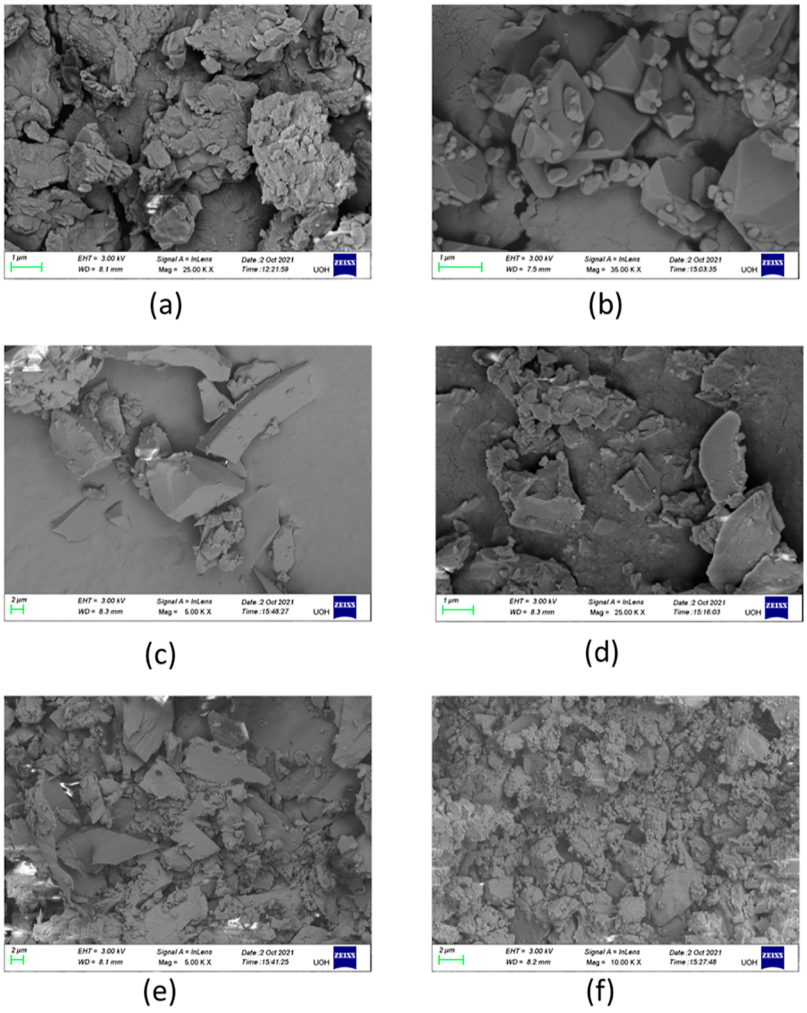

Figure 5. FESEM image of particles. (a) DBF-free base, (b) undissolved DBF residue under the equilibrium slurry medium at pH 1.2, (c) PAN-free base, (d) undissolved PAN residue under the equilibrium slurry medium at pH 1.2, (e) $DBF^{-}{\cdot}PAN^{+}$ scale-up batch, and (f) $DBF^{-}{\cdot}PAN^{+}$ residue under the equilibrium slurry medium at pH 1.2.

ment after 20 min. In contrast, neat PAN formed a sticky mass in the equilibrium solubility medium and the dried solid showed a unique PXRD pattern which indicated its phase conversion under a pH 1.2 buffer solution (Figure S9 in the Supporting Information). We surmise that with two secondary amines in PAN, indole NH (pK_a = 8.4) and aliphatic NH (pK_a = 9.0), the formation of a hydrochloride salt is likely.[41,42] Therefore, in case of neat PAN, because of the high solubility of even the product phase (named as PAN·HCl), it showed a continuous increase in the cumulative amount of dissolved drug (Figure 7a). The $DBF^{-}{\cdot}PAN^{+}$ salt was stable enough under the dissolution medium, and there was no significant phase transformation of the undissolved pellet up to 3 h. However, the equilibrium solubility of $DBF^{-}{\cdot}PAN^{+}$ salt at 48 h in pH 1.2 gave a precipitate residue which showed a new phase of $DBF^{-}{\cdot}PAN^{+}$ salt (Figure S10 in the Supporting Information), indicating its short period stability under a pH 1.2 solution (up to 24 h).

Even though it is interesting to note the high dissolution rate of the $DBF^{-}{\cdot}PAN^{+}$ salt with respect to both the individual drugs, there is subsaturation reached at an earlier time point for DBF during dissolution, and it shows a continuous rise in drug concentration with respect to PAN such that the dissolution profiles become more divergent with the time but eventually reach similar saturation values (Figure 7b). This phenomenon could be understood from the dissolution curve of neat forms which showed a quick equilibrium achieved between the release rate and precipitation rate in case of DBF and a comparatively slower profile in case of PAN. With a 1:1 salt stoichiometry, the $DBF^{-}{\cdot}PAN^{+}$ salt will release both drug counter ions simultaneously in the dissolution medium, yet the concentrations of DBF and PAN were observed to be different. Under this situation of dissolution and solubility, a plausible mechanism for the $DBF^{-}{\cdot}PAN^{+}$ salt concentration profile and dissociation pathway is shown in Figure 8. The release of the $DBF^{-}{\cdot}PAN^{+}$ salt in solution in the form of tight ion pairs was followed by its disproportionation into individual components, which in turn partially precipitated in their new phases as DBF·MH and PAN·HCl. Simultaneously, there is a possibility of establishing an equilibrium between a tight ion pair of dissolved $DBF^{-}{\cdot}PAN^{+}$ and its precipitated new form under a saturated solution (as observed in the equilibrium solubility experiment). Since the solubility of DBF·MH is very poor, the total content of DBF species in solution is always lower than that of PAN, as observed in the cumulative drug concentration experiment (Figure 7a). Consequently, the dissolution profile of the $DBF^{-}{\cdot}PAN^{+}$ salt with respect to DBF always lags with the dissolution profile of PAN. Since prolonged incubation of

https://doi.org/10.1021/acsomega.3c01881
ACS Omega 2023, 8, 18255−18265

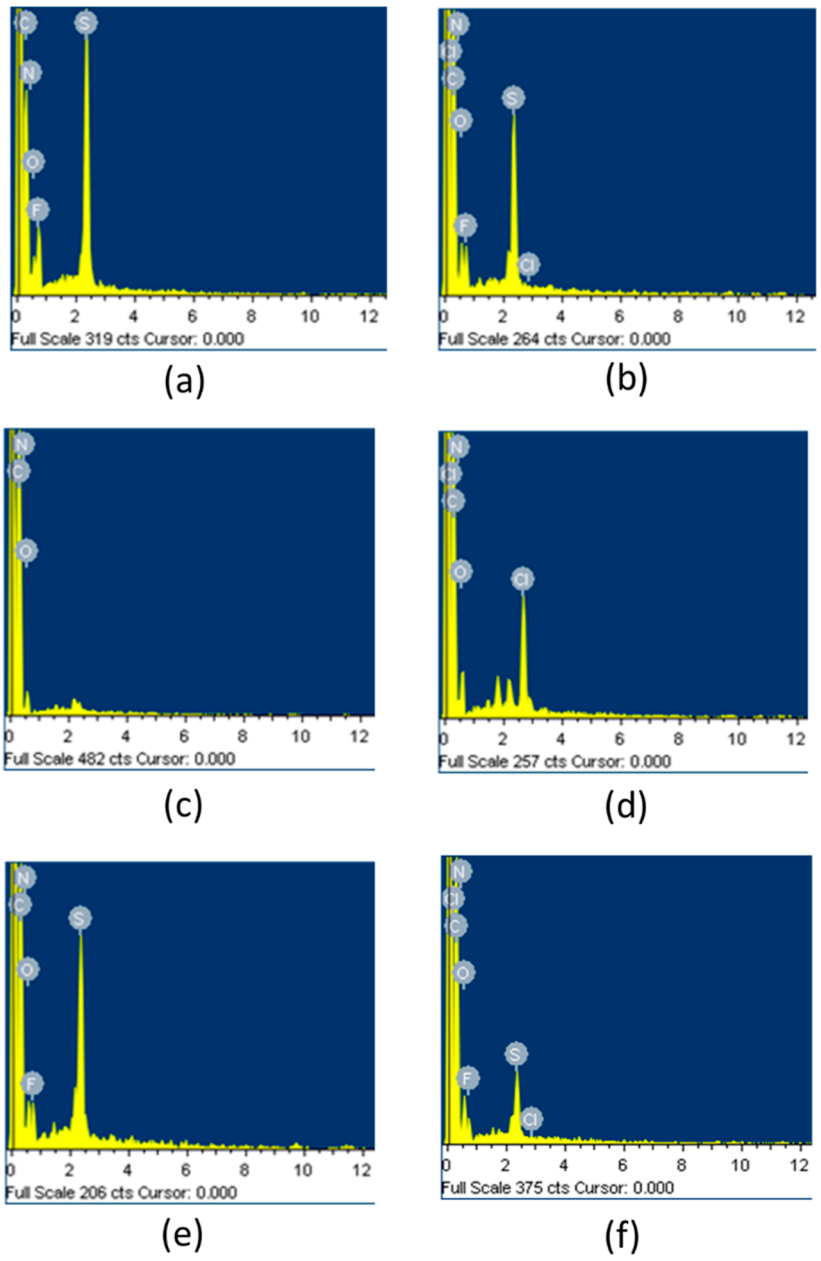

Figure 6. FESEM-EDX plot for the characterization of chloride content where the x-axis represents energy (in keV) and the y-axis represents the counts. (a) DBF-free base, (b) undissolved DBF under the equilibrium slurry medium at pH 1.2, (c) PAN-free base, (b) undissolved PAN under the equilibrium slurry medium at pH 1.2, (e) $DBF^{-}{\cdot}PAN^{+}$ scale-up batch, and (f) undissolved $DBF^{-}{\cdot}PAN^{+}$ under the equilibrium slurry medium at pH 1.2.

the $DBF^{-}{\cdot}PAN^{+}$ salt under a pH 1.2 buffer solution converted to a new phase, it was important to analyze the phase of the remaining solid left at the end of the dissolution experiment. Comparison of the PXRD pattern of the latter solid with the DBF·MH, PAN·HCl, and $DBF^{-}{\cdot}PAN^{+}$ salts suggested that the remaining solid had a mixture of original $DBF^{-}{\cdot}PAN^{+}$ salt and its new phase along with the traces of DBF·MH and PAN·HCl (Figure S11 in the Supporting Information). This evidence suggested that phase conversion and disproportionation started at the exposed surface of the pellet which corroborates the proposed mechanism for the dissolution profile of the $DBF^{-}{\cdot}PAN^{+}$ salt (Figures 7 and 8).

2.4. Biological Evaluation of $DBF^{-}{\bullet}PAN^{+}$. Analysis of the effect of drug combination on biological efficacy is of utmost interest for a drug−drug cocrystal in the frame of pharmaceutical crystal engineering.[43,44] Although it has already been investigated in vitro and in vivo that cotreatment with an HDACi and BRAFi in a certain concentration range synergistically induces cell death in resistant $BRAF^{V600E}$ melanoma cells, it would be remarkable to evaluate this in a stoichiometric cocrystal as a fixed-dose formulation.[28,35] Here, the use of HDACi is to keep the mitogen-activated protein kinase (MAPK) pathway inactive in response to BRAFi, thereby inducing caspase-dependent apoptotic cell death in resistant cells. Since the BRAF gene is commonly involved in normal processes of cell growth and differentiation, we have performed the cytotoxicity and apoptosis experiments of DBF, PAN, and $DBF^{-}{\cdot}PAN^{+}$ in ovarian cancer cell lines (i.e., A2780, 2008, and their cisplatin-resistant counterparts A2780/CP and C13*) where mutant BRAF is absent as well as in the melanoma

https://doi.org/10.1021/acsomega.3c01881
ACS Omega 2023, 8, 18255−18265

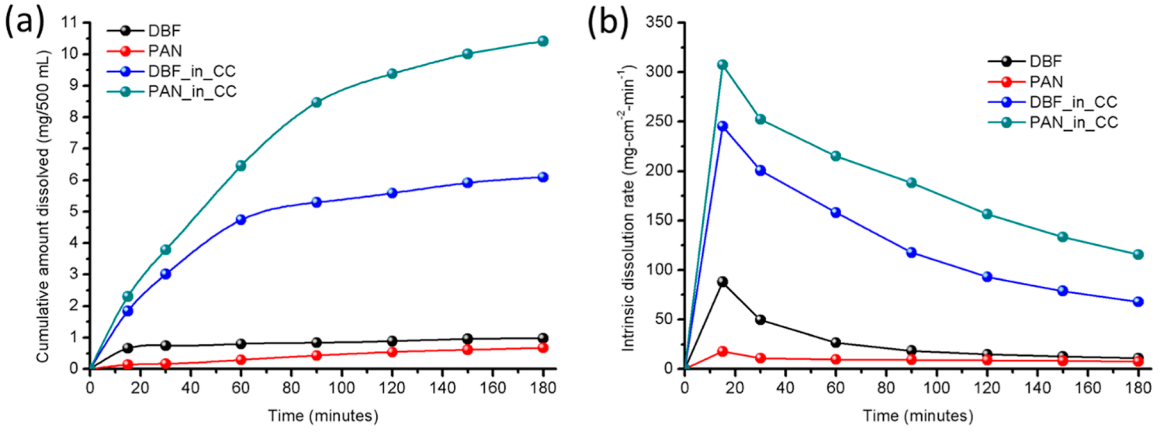

Figure 7. Dissolution profile of DBF, PAN, and DBF^{-}·PAN^{+} salts in the pH 1.2 (0.1 N HCl) buffer. (a) Cumulative amount dissolved in 500 mL and (b) IDR of neat DBF, neat PAN, and DBF^{-}·PAN^{+} with respect to DBF (in cocrystal CC) and PAN (in CC).

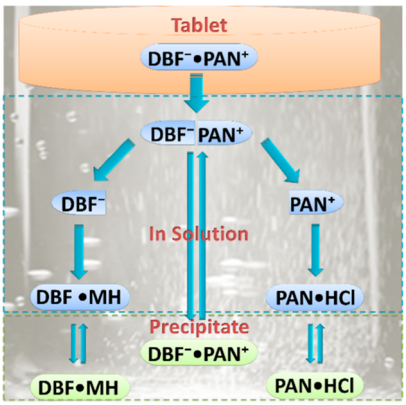

Figure 8. Plausible mechanism for dissolution of DBF^{-}·PAN^{+} which shows a tight ion pair in the aqueous solution followed by isolation of solvated ions which partially converted to DBF·MH and PAN·HCl during precipitation.

metastatic cell line Sk-Mel28 which expresses mutant BRAF^{V600E}.

A cytotoxicity assay was performed for neat DBF, marketed saline formulation of DBF (i.e., the mesylate salt DBF·MS), neat PAN, and DBF^{-}·PAN^{+}. As shown in Figure 9, neat DBF and DBF·MS have similar dose−response in all cell lines in the micromolar range, but the IC_{50} values are lower in ovarian cell lines compared to the melanoma metastatic cell line Sk-Mel28 (Figure S12 and Table S3 in the Supporting Information). However, PAN inhibits ovarian cancer cell lines at much lower concentrations (i.e., IC_{50} range ∼4−9 nM) compared to the Sk-Mel28 cell line (IC_{50} = 45.3 ± 12.0 nM). It is remarkable to observe that cell inhibition activity of DBF^{-}·PAN^{+} in ovarian cancer cell lines is not appreciable, and it shows either comparable activity (in 2008 and C13* cells) or even poor (in A2780 and A2780/CP) activity to PAN itself. This indicates that cotreatment does not improve cell proliferation inhibition in ovarian cancer cells. However, DBF^{-}·PAN^{+} shows a better response in the melanoma Sk-Mel28 cells, specifically in the range of 25−50 nM concentration, which shows approximately 2-fold lower IC_{50} value (21.9 ± 7.2 nM) than that of neat PAN (45.3 ± 12.0 nM). These results suggest that the combination drug DBF^{-}·PAN^{+} salt complex not only reduces dose−response from micromolar (μM) to nanomolar (nM) (3 log units) but also lowers the IC_{50} to half that of PAN in melanoma Sk-Mel28 cells.

To assess whether a possible perturbation of the distribution of cells in the different phases of the cell cycle underlies the antiproliferative activity, the compounds were tested in cytofluorimetric experiments on the 2008, C13*, and Sk-Mel28 cell lines. Cell-cycle analysis was performed after 48 h of incubation, and the working concentrations of compounds were fixed approximately at the respective IC_{50} values. Distribution of cells in the different phases of the cell cycle and in the amount of apoptotic hypodiploid cells after treatment with drug molecules are shown in Figure 9b,d,f. The percentage of cells in the different phases of the cell cycle is given in Table 1. Untreated cells showed a normal diploid distribution presenting fast proliferation characteristics. DBF caused a decrease of cell distribution in the S- and G_2/M-phases according to a recent report, accompanied by an almost 4-fold increase of hypodiploid cells in all three cell lines.[45] This apoptotic effect was even much more remarkable with both PAN (as also reported in other ovarian cancer cell lines) and DBF^{-}·PAN^{+} in all cell lines, reaching the 30−40% of hypodiploid cells and a concomitant reduction of cells in the G_0G_1-phase.[46] In our experimental conditions, this treatment greatly deranged the cell-cycle phase distribution of all cell lines. Notably, while PAN and DBF^{-}·PAN^{+} had the same effect in 2008 cells, DBF^{-}·PAN^{+} was almost doubly effective than PAN alone in the resistant counterpart C13* cells and in melanoma Sk-Mel28 cells, causing a great reduction of cells in all phases, in particular the G_0G_1-phase, which was coupled to a huge increase of cell population in the sub-G_1-phase, which exceeded the 80% and is indicative of great apoptotic cell death.

This massive induction of apoptotic cell death resulting from the analysis of the cell cycle was thus further analyzed by the annexin-V fluorescein isothiocyanate (FITC)/propidium iodide (PI) method (Table S4 in the Supporting Information). Since the percentage of cells positive to annexin-V is greater than those positive to both annexin-V and PI, we deduce that the main effect of each treatment, namely, that of PAN and DBF^{-}·PAN^{+}, was to cause early apoptosis and even if to a lesser extent, late apoptosis. Again, the effect of PAN was amplified in the case of DBF^{-}·PAN^{+} to values always higher in resistance than in sensitive cells, accounting, at least in part, for the improvement of some IC_{50} values. In fact, while PAN alone was more active only in A2780/CP cells than in the sensitive counterpart, DBF^{-}·PAN^{+} caused an apoptotic effect at least double in all resistant lines compared to sensitive ones.

https://doi.org/10.1021/acsomega.3c01881
ACS Omega 2023, 8, 18255−18265

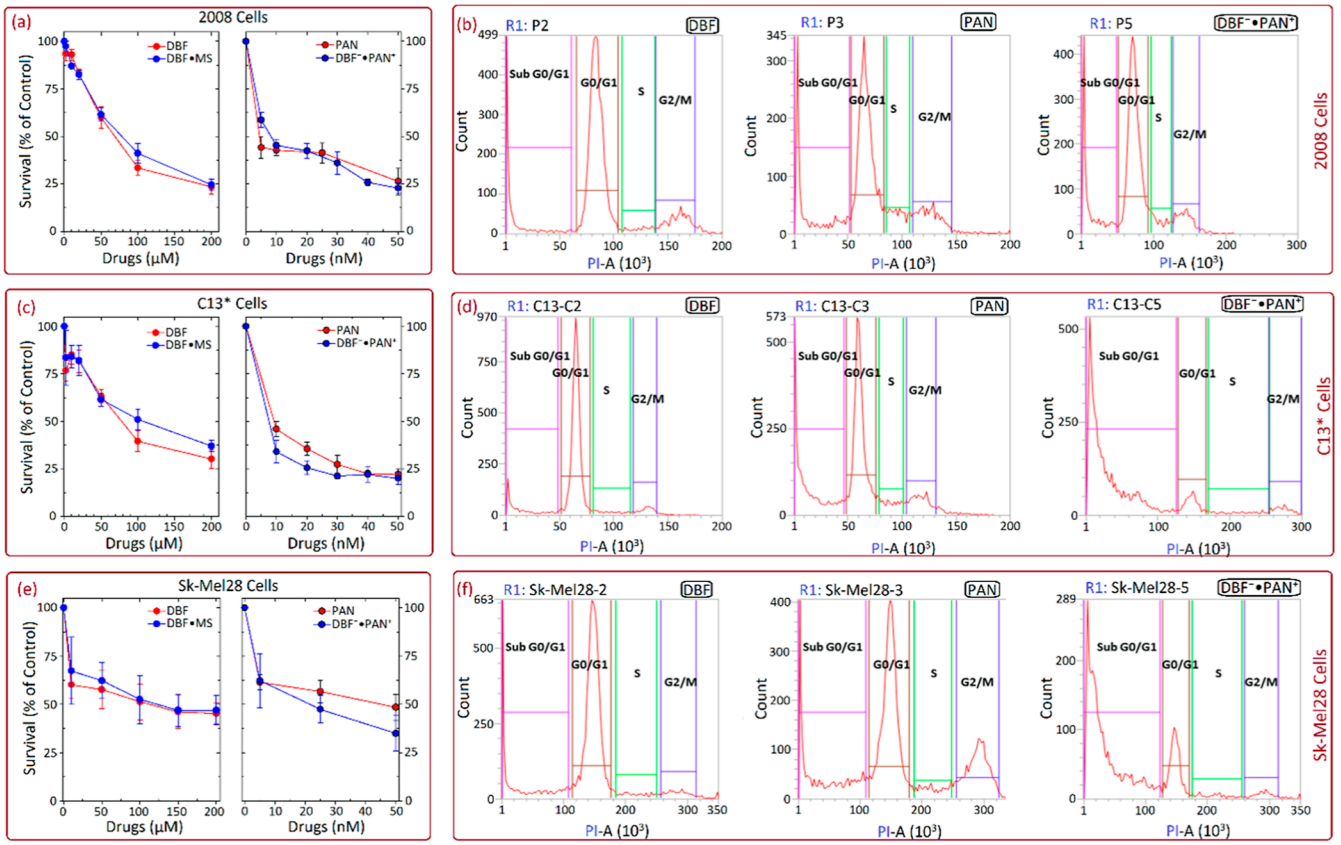

Figure 9. (a) Inhibition of cell growth in 2008 cells, (b) cell cycle-related analysis for 2008 cells after treatment with drugs, (c) inhibition of cell growth in the cisplatin-resistant counterpart of 2008 cells (i.e., C13* cells), (d) cell cycle-related analysis for the C13* cells after treatment with drugs, (e) inhibition of cell growth in the human melanoma cancer cells Sk-Mel28, and (f) cell cycle-related analysis for Sk-Mel28 after treatment with drugs. Cell survival percentages are the mean ± SEM of three separate experiments performed in duplicate for 2008 cells and C13* cells; however, two separate experiments were performed in duplicate for the human melanoma cancer cells Sk-Mel28. PI-A represents the propidium iodide area.

Table 1. Effect of DBF, PAN, and DBF^{-}·PAN^{+} on the Cell-Cycle Phase Distribution for 48 h on 2008, C13*, and Sk-Mel28 Cell Lines[a]

	2008 cells				C13* cells				Sk-Mel28 cells			
	G_0G_1	S	G_2/M	hypodiploid	G_0G_1	S	G_2/M	hypodiploid	G_0G_1	S	G_2/M	hypodiploid
Control	75.28	6.15	11.84	4.82	65.81	13.86	12.27	4.17	62.56	7.19	11.07	13.23
DBF	63.91	3.53	10.76	19.32	68.48	4.60	5.28	19.32	65.11	3.95	4.53	23.46
PAN	37.98	6.78	9.99	42.32	47.46	6.85	10.27	30.15	42.53	5.17	18.73	30.07
DBF^{-}·PAN^{+}	40.50	4.21	7.09	45.54	5.93	2.82	3.09	87.94	8.11	1.38	1.39	88.51

[a]Percentage distribution of the cell population in different phases was measured using flow cytometry analysis.

3. CONCLUSIONS

The present study has led to a clear conclusion that cocrystallization of DBF with PAN using mechanochemistry followed by structure determination by single-crystal X-ray diffraction indicates binary salt formation where an acidic proton transfer occurs from DBF to PAN, named DBF^{-}·PAN^{+}. Dissolution measurement under simulated gastric pH 1.2 (0.1 N HCl) showed that DBF^{-}·PAN^{+} is a fast-dissolving salt than either of the two drug species, and the salt profile is significantly higher than that of the individual dissolution rates. Due to the instability of DBF and PAN and the comparatively stable nature of DBF^{-}·PAN^{+} under a pH 1.2 buffer solution, a phase conversion was observed for all the drug compounds, but the transformation was moderate for DBF^{-}·PAN^{+}. Consequently, the apparent dissolution rate of DBF^{-}·PAN^{+} was compared with DBF and PAN, which showed a faster rate with respect to PAN because of its high solubility (as PAN·HCl) compared to DBF (as DBF·MH). Furthermore, in continuation of other reported studies on combination analysis of HDACi and BRAFi,[35] for the first time, a novel drug−drug combination in a fixed-stoichiometry salt (or "FDC") is analyzed for in vitro inhibition in BRAF^{V600E} melanoma cells. DBF^{-}·PAN^{+} shows improved inhibition in the melanoma cells which not only reduces dose−response from micromolar to nanomolar concentrations but also lowers the IC_{50} by half of that of PAN alone. Additionally, cell cycle analysis shows that PAN alone induces early apoptotic cell death in all resistant cells; however, its effect is amplified in the case of DBF^{-}·PAN^{+}, and consequently, IC_{50} reduces to half the value of PAN in resistant BRAF^{V600E} melanoma cells. This work provides a basis for in vivo and clinical studies of DBF^{-}·

https://doi.org/10.1021/acsomega.3c01881
ACS Omega 2023, 8, 18255−18265

PAN^{+} as an FDC formulation for acquired resistance against BRAF^{V600E} melanoma therapy, which may be translated to a potential combination supramolecular drug complex of high bioavailability.[47]

■ ASSOCIATED CONTENT

Supporting Information

The Supporting Information is available free of charge at https://pubs.acs.org/doi/10.1021/acsomega.3c01881.

Experimental section, ORTEP diagram and geometrical parameters of potential intra- and intermolecular interactions; stack plots of PXRD comparison, and DSC thermogram; and biological assays and related data (PDF)

Crystallographic information for CCDC 2057496 (CIF)

■ AUTHOR INFORMATION

Corresponding Authors

Sunil K. Rai − *Department of Chemistry, Faculty of Science, University of Lucknow, Lucknow 226025 Uttar Pradesh, India; Organic Chemistry Division, CSIR-National Chemical Laboratory (NCL), Pune 411 008 Maharashtra, India;* orcid.org/0000-0001-5509-3142; Email: sunilbhu28@gmail.com

Ashwini K. Nangia − *Organic Chemistry Division, CSIR-National Chemical Laboratory (NCL), Pune 411 008 Maharashtra, India; School of Chemistry, University of Hyderabad, Hyderabad 500 046, India;* orcid.org/0000-0003-2442-7255; Email: ashwini.nangia@gmail.com

Authors

Gaetano Marverti − *Department of Biomedical, Metabolic and Neural Sciences, University of Modena and Reggio Emilia, 41125 Modena, Italy*

Anilkumar Gunnam − *School of Chemistry, University of Hyderabad, Hyderabad 500 046, India*

Suryanarayana Allu − *School of Chemistry, University of Hyderabad, Hyderabad 500 046, India*

Complete contact information is available at: https://pubs.acs.org/10.1021/acsomega.3c01881

Notes

The authors declare no competing financial interest.

■ ACKNOWLEDGMENTS

S.K.R. thanks SERB, New Delhi, India, for the financial support (N-PDF fellowship 2016/001632) and CSIR-NCL, Pune, India, for providing the infrastructure to carry out this work. A.K.N. thanks for the financial and infrastructure support from the University Grants Commission, New Delhi (through the UPE and CAS programs), the Department of Science and Technology, New Delhi (through the PURSE and FIST programs), and the JC Bose Fellowship scheme (SR/S2/JCB-06/2009). G.M. thanks Laboratorio Dipartimentale Cell-Lab "Paolo Buffa", University of Modena and Reggio Emilia, Italy, for providing the cell culture and flow cytometry analysis facilities.

■ REFERENCES

(1) Stolk, R. P.; Rosmalen, J. G.; Postma, D. S.; de Boer, R. A.; Navis, G.; Slaets, J. P. J.; Ormel, J.; Wolffenbuttel, B. H. R.; Wolffenbuttel, B. H. Universal Risk Factors for Multifactorial Diseases: LifeLines: A Three-generation Population-based Study. *Eur. J. Epidemiol.* **2008**, *23*, 67−74.

(2) Zimmet, P.; Alberti, K. G. M. M.; Shaw, J. Global and Societal Implications of the Diabetes Epidemic. *Nature* **2001**, *414*, 782−787.

(3) Scrivo, R.; Vasile, M.; Bartosiewicz, I.; Valesini, G. Inflammation as "Common soil" of the Multifactorial Diseases. *Autoimmun. Rev.* **2011**, *10*, 369−374.

(4) Jha, V.; Garcia-Garcia, G.; Iseki, K.; Li, Z.; Naicker, S.; Plattner, B.; Saran, R.; Wang, A. Y.; Yang, C. W. Chronic Kidney Disease: Global Dimension and Perspectives. *Lancet* **2013**, *382*, 260−272.

(5) Torre, L. A.; Bray, F.; Siegel, R. L.; Ferlay, J.; Lortet-Tieulent, J.; Jemal, A. Global Cancer Statistics. *Ca-Cancer J. Clin.* **2015**, *65*, 87−108.

(6) Dahlöf, B. Cardiovascular Disease Risk Factors: Epidemiology and Risk Assessment. *Am. J. Cardiol.* **2010**, *105*, 3A−9A.

(7) Batus, M.; Waheed, S.; Ruby, C.; Petersen, L.; Bines, S. D.; Kaufman, H. L. Optimal Management of Metastatic Melanoma: Current Strategies and Future Directions. *Am. J. Clin. Dermatol.* **2013**, *14*, 179−194.

(8) Leiter, U.; Garbe, C. Epidemiology of Melanoma and Nonmelanoma Skin Cancer. The Role of Sunlight. *Adv. Exp. Med. Biol.* **2008**, *624*, 89−103.

(9) Siegel, R. L.; Miller, K. D.; Jemal, A. Cancer Statistics. *Ca-Cancer J. Clin.* **2019**, *69*, 7−34.

(10) Galata, C.; Wimmer, E.; Kasper, B.; Wenz, F.; Reißfelder, C.; Jakob, J. Multidisciplinary Tumor Board Recommendations for Oligometastatic Malignancies: A Prospective Single-Center Analysis. *Oncol. Res. Treat.* **2019**, *42*, 87−94.

(11) Anand, P.; Kunnumakara, A. B.; Sundaram, C.; Harikumar, K. B.; Tharakan, S. T.; Lai, O. S.; Sung, B.; Aggarwal, B. B. Cancer is a Preventable Disease that Requires Major Lifestyle Changes. *Pharm. Res.* **2008**, *25*, 2097−2116.

(12) Goffin, J.; Lacchetti, C.; Ellis, P. M.; Ung, Y. C.; Evans, W. K. First-line Systemic Chemotherapy in the Treatment of Advanced Non-small Cell Lung Cancer: A Systematic Review. *J. Thorac. Oncol.* **2010**, *5*, 260−274.

(13) Finn, R. S.; Crown, J. P.; Lang, I.; Boer, K.; Bondarenko, I. M.; Kulyk, S. O.; Ettl, J.; Patel, R.; Pinter, T.; Schmidt, M.; Shparyk, Y.; Thummala, A. R.; Voytko, N. L.; Fowst, C.; Huang, X.; Kim, S. T.; Randolph, S.; Slamon, D. J. The Cyclin-dependent Kinase 4/6 Inhibitor Palbociclib in Combination with Letrozole Versus Letrozole Alone as First-line Treatment of Oestrogen Receptor-positive, HER2-negative, Advanced Breast Cancer (PALOMA-1/TRIO-18): A Randomised Phase 2 Study. *Lancet Oncol* **2015**, *16*, 25−35.

(14) Haj Mohammad, N.; Ter Veer, E.; Ngai, L.; Mali, R.; van Oijen, M. G. H.; van Laarhoven, H. W. M. Optimal First-line Chemotherapeutic Treatment in Patients with Locally Advanced or Metastatic Esophagogastric Carcinoma: Triplet Versus Doublet Chemotherapy: A Systematic Literature Review and Meta-analysis. *Cancer Metastasis Rev* **2015**, *34*, 429−441.

(15) Joo, W. D.; Visintin, I.; Mor, G. Targeted Cancer Therapy. Are the Days of Systemic Chemotherapy Numbered? *Maturitas* **2013**, *76*, 308−314.

(16) Wabel, A. B.; Khajah, M. The Principles Behind Targeted Therapy for Cancer Treatment. In *Tumor Progression and Metastasis*; IntechOpen, 2019.

(17) Davies, H.; Bignell, G.; Cox, C.; Stephens, P.; Edkins, S.; Clegg, S.; Teague, J.; Woffendin, H.; Garnett, M.; Bottomley, W.; Davis, N.; Dicks, E.; Ewing, R.; Floyd, Y.; Gray, K.; Hall, S.; Hawes, R.; Hughes, J.; Kosmidou, V.; Menzies, A.; Mould, C.; Parker, A.; Stevens, C.; Watt, S.; Hooper, S.; Wilson, R.; Jayatilake, H.; Gusterson, B.; Cooper, C.; Shipley, J.; Hargrave, D.; Pritchard-Jones, K.; Maitland, N.; Chenevix-Trench, G.; Riggins, G.; Bigner, D.; Palmieri, G.; Cossu, A.; Flanagan, A.; Nicholson, A.; Ho, J.; Leung, S.; Yuen, S.; Weber, B.; Seigler, H.; Darrow, T.; Paterson, H.; Marais, R.; Marshall, C.; Wooster, R.; Stratton, M.; Futreal, P. Mutations of the BRAF Gene in Human Cancer. *Nature* **2002**, *417*, 949−954.

(18) Hatzivassiliou, G.; Song, K.; Yen, I.; Brandhuber, B. J.; Anderson, D. J.; Alvarado, R.; Ludlam, M. J. C.; Stokoe, D.; Gloor, S.

L.; Vigers, G.; Morales, T.; Aliagas, I.; Liu, B.; Sideris, S.; Hoeflich, K. P.; Jaiswal, B. S.; Seshagiri, S.; Koeppen, H.; Belvin, M.; Friedman, L. S.; Malek, S. RAF Inhibitors Prime Wild-type RAF to Activate the MAPK Pathway and Enhance Growth. *Nature* **2010**, *464*, 431−435.
(19) Holderfield, M.; Deuker, M. M.; McCormick, F.; McMahon, M. Targeting RAF Kinases for Cancer Therapy: BRAF-mutated Melanoma and Beyond. *Nat. Rev. Cancer* **2014**, *14*, 455−467.
(20) Bollag, G.; Tsai, J.; Zhang, J.; Zhang, C.; Ibrahim, P.; Nolop, K.; Hirth, P. Vemurafenib: The First Drug Approved for BRAF-mutant Cancer. *Nat. Rev. Drug. Discov.* **2012**, *11*, 873−886.
(21) Rheault, T. R.; Stellwagen, J. C.; Adjabeng, G. M.; Hornberger, K. R.; Petrov, K. G.; Waterson, A. G.; Dickerson, S. H.; Mook, R. A., Jr.; Laquerre, S. G.; King, A. J.; et al. Discovery of Dabrafenib: A Selective Inhibitor of Raf Kinases with Antitumor Activity against BRaf-Driven Tumors. *ACS Med. Chem. Lett.* **2013**, *4*, 358−362.
(22) Nikolaou, V. A.; Stratigos, A. J.; Flaherty, K. T.; Tsao, H. Melanoma: New Insights and New Therapies. *J. Invest. Dermatol.* **2012**, *132*, 854−863.
(23) Das Thakur, M.; Salangsang, F.; Landman, A. S.; Sellers, W. R.; Pryer, N. K.; Levesque, M. P.; Dummer, R.; McMahon, M.; Stuart, D. D. Modelling Vemurafenib Resistance in Melanoma Reveals a Strategy to Forestall Drug Resistance. *Nature* **2013**, *494*, 251−255.
(24) He, B.; Lu, C.; Zheng, G.; He, X.; Wang, M.; Chen, G.; Zhang, G.; Lu, A. Combination Therapeutics in Complex Diseases. *J. Cell. Mol. Med.* **2016**, *20*, 2231−2240.
(25) Mokhtari, R. B.; Homayouni, T. S.; Baluch, N.; Morgatskaya, E.; Kumar, S.; Das, B.; Yeger, H. Combination Therapy in Combating Cancer. *Oncotarget* **2017**, *8*, 38022−38043.
(26) Robert, C.; Grob, J. J.; Stroyakovskiy, D.; Karaszewska, B.; Hauschild, A.; Levchenko, E.; Chiarion Sileni, V.; Schachter, J.; Garbe, C.; Bondarenko, I.; Gogas, H.; Mandalá, M.; Haanen, J. B. A. G.; Lebbé, C.; Mackiewicz, A.; Rutkowski, P.; Nathan, P. D.; Ribas, A.; Davies, M. A.; Flaherty, K. T.; Burgess, P.; Tan, M.; Gasal, E.; Voi, M.; Schadendorf, D.; Long, G. V. Five-Year Outcomes with Dabrafenib plus Trametinib in Metastatic Melanoma. *New Engl. J. Med.* **2019**, *381*, 626−636.
(27) Kanemaru, Y.; Natsumeda, M.; Okada, M.; Saito, R.; Kobayashi, D.; Eda, T.; Watanabe, J.; Saito, S.; Tsukamoto, Y.; Oishi, M.; Saito, H.; Nagahashi, M.; Sasaki, T.; Hashizume, R.; Aoyama, H.; Wakai, T.; Kakita, A.; Fujii, Y. Dramatic Response of BRAF V600E-mutant Epithelioid Glioblastoma to Combination Therapy with BRAF and MEK Inhibitor: Establishment and Xenograft of a Cell Line to Predict Clinical Efficacy. *Acta Neuropathol. Commun.* **2019**, *7*, 119.
(28) Gallagher, S. J.; Gunatilake, D.; Beaumont, K. A.; Sharp, D. M.; Tiffen, J. C.; Heinemann, A.; Weninger, W.; Haass, N. K.; Wilmott, J. S.; Madore, J.; Ferguson, P. M.; Rizos, H.; Hersey, P. HDAC Inhibitors Restore BRAF-inhibitor Sensitivity by Altering PI3K and Survival Signalling in a Subset of Melanoma. *Int. J. Cancer* **2018**, *142*, 1926−1937.
(29) Carson, R.; Celtikci, B.; Fenning, C.; Javadi, A.; Crawford, N.; Perez-Carbonell, L.; Lawler, M.; Longley, D. B.; Johnston, P. G.; Van Schaeybroeck, S. HDAC Inhibition Overcomes Acute Resistance to MEK Inhibition in BRAF-mutant Colorectal Cancer by Down-regulation of c-FLIPL. *Clin. Cancer Res.* **2015**, *21*, 3230−3240.
(30) Thipparaboina, R.; Kumar, D.; Chavan, R. B.; Shastri, N. R. Multidrug Co-crystals: Towards the Development of Effective Therapeutic Hybrids. *Drug Discov. Today* **2016**, *21*, 481−490.
(31) Kwon, K. C.; Lee, C. Analysis of Fixed-Dose Combination Products Approved by the US Food and Drug Administration, 2010-2015: Implications for Designing a Regulatory Shortcut to New Drug Application. *Ther. Innov. Regul. Sci.* **2017**, *51*, 111−117.
(32) Oo, C.; Sy, S. K. Fixed-dose Combinations: A Potential Means to Boost Drug Development for Selected Drugs. *Drug Discov. Today* **2018**, *23*, 457−459.
(33) ENTRESTO (Sacubitril and Valsartan) Tablets, for Oral Use. Initial U.S. Approval: 2015, 2023 https://www.accessdata.fda.gov/drugsatfda_docs/label/2021/207620s018lbl.pdf. (Accessed March, 11, 2023).
(34) Eadie, A. L.; Brunt, K. R.; Herder, M. Exploring the Food and Drug Administration's Review and Approval of Entresto (Sacubitril/Valsartan). *Pharmacol. Res. Perspect.* **2021**, *9*, No. e00794.
(35) Lai, F.; Guo, S. T.; Jin, L.; Jiang, C. C.; Wang, C. Y.; Croft, A.; Chi, M. N.; Tseng, H.-Y.; Farrelly, M.; Atmadibrata, B.; Norman, J.; Liu, T.; Hersey, P.; Zhang, X. D. Cotargeting Histone Deacetylases and Oncogenic BRAF Synergistically Kills Human Melanoma Cells by Necrosis Independently of RIPK1 and RIPK3. *Cell Death Dis* **2013**, *4*, No. e655.
(36) Rai, S. K.; Gunnam, A.; Mannava, M. K. C.; Nangia, A. K. Improving the Dissolution Rate of the Anticancer Drug Dabrafenib. *Cryst. Growth Des.* **2020**, *20*, 1035−1046.
(37) Etter, M. C. Encoding and Decoding Hydrogen-bond Patterns of Organic Compounds. *Acc. Chem. Res.* **1990**, *23*, 120−126.
(38) Desiraju, G. R. Crystal Engineering: From Molecule to Crystal. *J. Am. Chem. Soc.* **2013**, *135*, 9952−9967.
(39) Haskins, M. M.; Zaworotko, M. J. Screening and Preparation of Cocrystals: A Comparative Study of Mechanochemistry vs Slurry Methods. *Cryst. Growth Des.* **2021**, *21*, 4141−4150.
(40) Teleki, A.; Nylander, O.; Bergström, C. A. Intrinsic Dissolution Rate Profiling of Poorly Water-soluble Compounds in Biorelevant Dissolution Media. *Pharmaceutics* **2020**, *12*, 493.
(41) Hamed, R.; Awadallah, A.; Sunoqrot, S.; Tarawneh, O.; Nazzal, S.; AlBaraghthi, T.; Al Sayyad, J.; Abbas, A. pH-Dependent Solubility and Dissolution Behavior of Carvedilol. Case Example of a Weakly Basic BCS Class II Drug. *AAPS PharmSciTech* **2016**, *17*, 418−426.
(42) Australian Public Assessment Report for Panobinostat lactate. 2023 https://www.tga.gov.au/sites/default/files/auspar-panobinostat-lactate-181022.pdf (Accessed on March 11, 2023).
(43) Thakuria, R.; Sarma, B. Drug-drug and Drug-nutraceutical Cocrystal/Salt as Alternative Medicine for Combination Therapy: A Crystal Engineering Approach. *Crystals* **2018**, *8*, 101.
(44) Wang, X.; Du, S.; Zhang, R.; Jia, X.; Yang, T.; Zhang, X. Drug-Drug Cocrystals: Opportunities and Challenges. *Asian J. Pharm. Sci.* **2021**, *16*, 307−317.
(45) Phadke, M.; Remsing Rix, L. L.; Smalley, I.; Bryant, A. T.; Luo, Y.; Lawrence, H. R.; Schaible, B. J.; Chen, Y. A.; Rix, U.; Smalley, K. S. M. Dabrafenib inhibits the growth of BRAF-WT cancers through CDK16 and NEK9 inhibition. *Mol. Oncol.* **2018**, *12*, 74−88.
(46) Helland, Ø.; Popa, M.; Bischof, K.; Gjertsen, B. T.; McCormack, E.; Bjørge, L. The HDACi Panobinostat Shows Growth Inhibition Both In Vitro and in a Bioluminescent Orthotopic Surgical Xenograft Model of Ovarian Cancer. *PLoS ONE* **2016**, *11*, No. e0158208.
(47) Bolla, G.; Sarma, B.; Nangia, A. K. Crystal Engineering of Pharmaceutical Cocrystals in the Discovery and Development of Improved Drugs. *Chem. Rev.* **2022**, *122*, 11514−11603.

https://doi.org/10.1021/acsomega.3c01881
ACS Omega 2023, 8, 18255−18265